5

Beam halo measurements using wire scanners

Prior to the diamond detector installation, a first attempt of beam halo measurements has been performed in 2013 using the currently installed wire scanners in the Extraction Line (EXT) and behind the IP (post-IP). Based on these measurements, the beam halo distribution was parametrised and compared with old measurements done in the past at the old EXT line of ATF [94]. Such parametrisation allow modelling of the beam halo which could be useful for the study of a transverse halo collimation system, aiming at reducing the background for the measurements using diamond detectors. In this chapter, the experimental setup and measurement procedures are described, measurement limitations are discussed, then data analysis procedure and measurement results are presented.

5.1 Experimental setup

5.1.1 EXT line wire scanners

In our experiment MW2X and MW3X wire scanners are used in the EXT line. The schematic layout of the wire scanners is presented in Section 3.3.3. A Cherenkov detector at around 26 m downstream of MW2X and 22 m downstream of MW3X is used to detect the bremsstrahlung photons generated by the wire scanners [95]. It should be noticed that in 2005 this Cherenkov detector was installed at around 5 m downstream of MW2X for the old EXT line [18].

For the measurements in the EXT line, where the vertical beam size is relatively small, as can be seen in Table 3.2, we used the 50 μm tungsten X wire for horizontal scan and the 10 μm tungsten Y wire for vertical scan. Before doing the experiment,

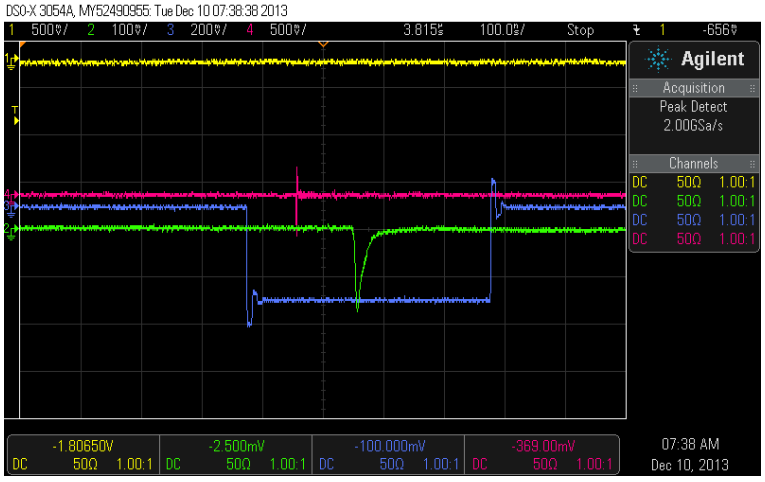

Figure 5.1: Output signal of voltage as a function of time (green) and gate width in ns (blue) for the PMT at Post-IPW

we checked the gate width and the timing [1] of the PMTs. As shown in Fig. 5.1, the gate width is 500 ns and the timing is 180 ns. The signal from the PMT is connected to a 14 bit charge sensitive ADC, which integrates the signal detected inside the gate and converts the charge into a number (for the ADC used the limits are from 0 to 16383). The pedestal is subtracted from the ADC output number in a program specially prepared for wire scanner control and data taking. In this program, the beam intensity detected by the Integrating Current Transformers (ICT) at the EXT line is recorded simultaneously while the wires are moving, so that the fluctuation of the wire signal caused by beam intensity variations can be corrected by renormalizing the wire signal to the beam intensity, either online or offline. Beam position correction can also be done manually by taking data from the Beam Position Monitors (BPMs) near the wire scanners. However, the resolution of the BPMs is around 10 to 20 μm, while the position jitter of beam is estimated to be 2.4 to 4.4 μm. Therefore the beam position jitter is not corrected in these measurements.

[1] The signal delay between the gate and the PMT

5.1.2 Post-IP wire scanners

The post-IP wire scanner (post-IPW) is located 75 cm downstream of the IP. It uses a plastic scintillator detector (BG monitor) at the same location as the photon detector used for the Shintake-monitor and is also connected to a PMT. The post-IPW has the same configuration and characteristics as the wire scanners at the EXT line (MW2X and MW3X), a picture of this device can be seen in Fig. 5.2. For the measurements with the post-IPW, the beam size is in the 100 μm range (see Table 3.2) therefore, we used 50 μm tungsten X and Y wires for horizontal and vertical scans, respectively. Before doing the experiment, we checked the gate width and the timing of the PMT finding 410 ns and 180 ns, respectively. An example of output signal pulse from the PMT at the post-IPW is shown in Fig. 5.1.

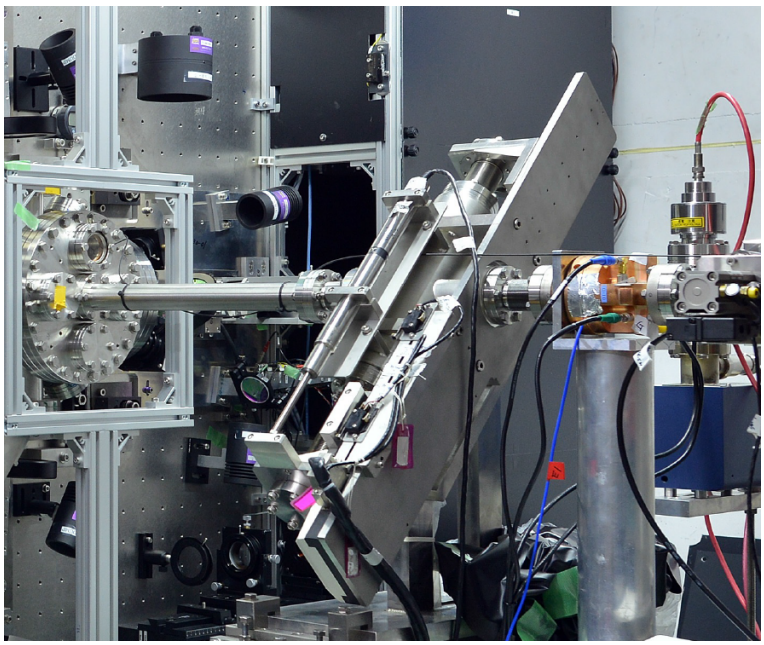

Figure 5.2: Post-IP wire scanner (photo taken in July 2013)

Furthermore, during the measurements using the post-IPW, we moved vertically the Tapered Beam Pipe (TBP) located at 28 m upstream of the IP to check the effect of this movement on the background level and beam halo distribution.

5.2 Limitations of wire scanners

The wire scanners at ATF2 were designed for performing beam size measurements. In each wire scanner eight wires are arranged next to each other (see Fig. 3.9). This fact could limit this device for beam halo measurements, because the measurements using one wire can be affected by the background noise generated by the interaction of beam halo with the other neighbouring wires. An example of scan from 0 to 80 mm is shown in Fig. 5.3. The data out of the background clearly indicate the wire positions. A normalization by $\sqrt{2}$ should be applied since the wire scanner is 45° with respect to the horizontal axis. Except for the first 50 μm Y wire, which is about 10 mm from the starting point of the scan, the measurements using the other wires are all affected by background from other wires.

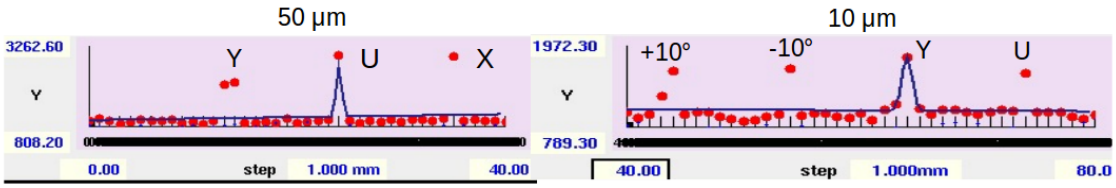

Figure 5.3: An example of scan from 0 to 80 mm using MW2X wire scanner with the corresponding wire positions

As the background generated by neighbouring wires depends both on their thickness and orientation, different background levels could lead to different limitations to the dynamic range of the wires used to probe the beam halo. This can be seen in the results presented in Fig. 5.7, where the 10 μm Y wire has a dynamic range of 7×10^3, and in Fig. 5.6 where the 50 μm X wire only has a dynamic range of 10^3. Moreover, the dynamic range of the measurement is limited by the gain of the PMTs and the 14 bit ADC used for the photon detection. Therefore, in order to get better resolution for the beam halo measurement, we first applied to the PMT the lowest voltage to measure the beam core and then the voltage was increased step by step to scan the beam halo (see Fig. 5.4 (upper)). The signal strength measured by the photon detectors is corrected by the total beam charge measured by the ICT to take into account the fluctuations in beam intensity. Furthermore, the data taken at higher voltages is normalized according to the overlap region with the data taken at lower voltages (see Fig. 5.4 (lower)). It should be noticed that at lower voltages, the PMT is not sensitive to the background

signal and the fluctuations in the flat parts are caused by the electronic noise, thus from the lowest voltage only the beam core data is considered (not the background level). The background level is extracted from the measurements at higher voltages. The normalization procedure is explained in more detail in Section 5.3.1.

5.3 Measurement results from 2013 campaign

Different sets of halo measurements were performed in April, June and December 2013 using MW2X in the EXT line and the post-IPW. During this runs the beam energy was 1.3 GeV and the optics configuration was: $10\beta_x^* \times 1\beta_y^*$. The intensity given in number of particles of the beam, the date, the wire scanner used and the kind of measurements (horizontal or vertical) taken at each run are summarized in Table 5.1. In this chapter only some of the measurements (corresponding the bolded dates) are presented. More detailed analyses and results can be found in Ref. [94].

Date	**Shift**	**ID run**	**N**	**Wire scanner**	**Axis**
10th of April	SWING	MW2X-10A-H	5×10^9	MW2X	H
16th of April	OWL	MW2X-16A-H	7×10^9	MW2X	H
		MW2X-16A-V	7×10^9		V
17th of April	SWING	Post-IPW-17A-H	7×10^9	Post-IP	H
		Post-IPW-17A-V	7×10^9		V
14th of June	DAY	Post-IPW-14J-V	1×10^9	Post-IP	V
12th of December	OWL	Post-IPW-12D-V	6×10^9	Post-IP	V

Table 5.1: Summary of 2013 halo measurements

5.3.1 Data acquisition and analysis

All of the data treatment has been done using the program root [96]. The acquisition and analysis of the data is performed as follows:

1. Data acquisition: For all the experiments the data were taken at different PMT voltages in order to be sensitive to the beam halo particles. Then the data corresponding to the lowest voltage was fitted with a Gaussian function plus a constant in order to determine the beam size and mean position as it is done in the ATF2 control room

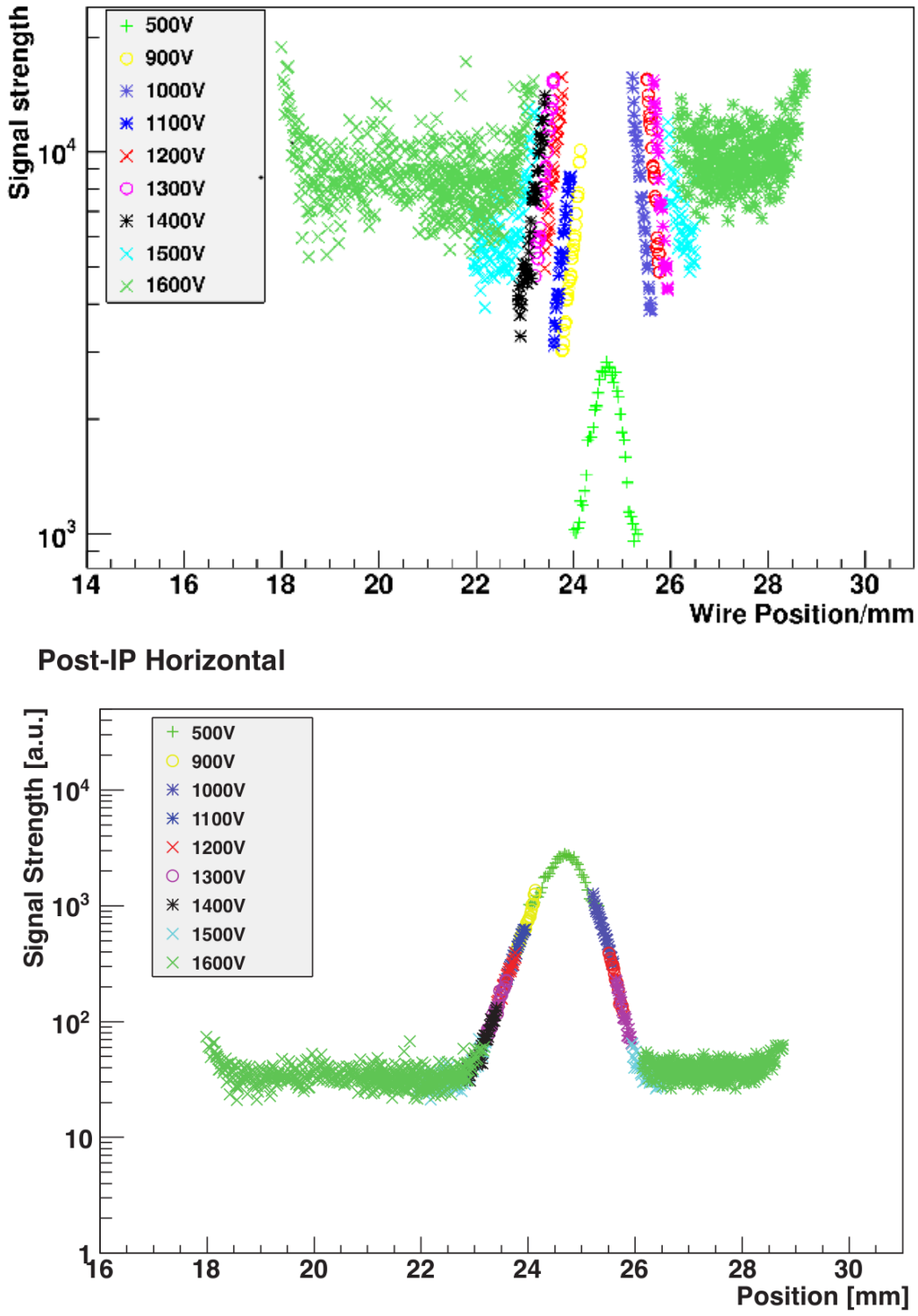

Figure 5.4: Example of a beam core and beam halo scan applying different voltages to the PMT before (upper) and after (lower) voltage normalization. The rise of signal strength on the two edge of data taken at 1600V is caused by the background signal from the surrounding wires

software in normal operation. The information is used afterwards to normalize the wire scanner position to the number of standard deviations of beam core (σ) from the beam center.

2. Data normalization:

- **Intensity normalization:** The data collected is corrected by the intensity of the beam given by the ICT to take into account beam charge changes during the run.
- **Wire orientation correction:** The wire position has to be corrected due to the orientation of the wire scanner (see Fig. 3.9), by dividing the wire position data by $\sqrt{2}$.
- **Number of σ normalization:** Then the data is normalized to the number of σ using the information calculated in step 1.
- **Voltage normalization:** In order to combine the data taken with different voltages we perform a normalization by defining the ratio between the lowest voltage data and other voltages data in the overlap region. Then all the data of a given voltage is divided by the ratio obtained for the corresponding voltage.

3. Data binning: In order to reduce the fluctuation of the data taken we performed a binning procedure. The bin size has to take into account the step of the wire scanner measurements in order to not have empty bins and the number of bins is chosen in order to minimize the reduced χ^2 of the fit. The criteria we followed was to accept the fits with values $0.5 < \chi^2/N_{DOF} < 3$ where $N_{DOF} = N_{bin} - 2$ is the degree of freedom. The value of each bin corresponds to the mean value of the points in this bin and the error bar correspond to the statistical error as the mean. Fig. 5.5 shows an example of data taken on the 10th of April of 2013 with (right) and without (left) binning the data.

4. Fitting range: Before data fitting, the fitting range should be defined. Following Suehara's parametrization (see Eq. 3.9 and Eq. 3.10) we try to fit for $3 < X < 6$ and for $X > 6$. However, for some cases, new ranges were defined in view of the data taken. In principle the two sides of the halo are supposed to be symmetric, however,

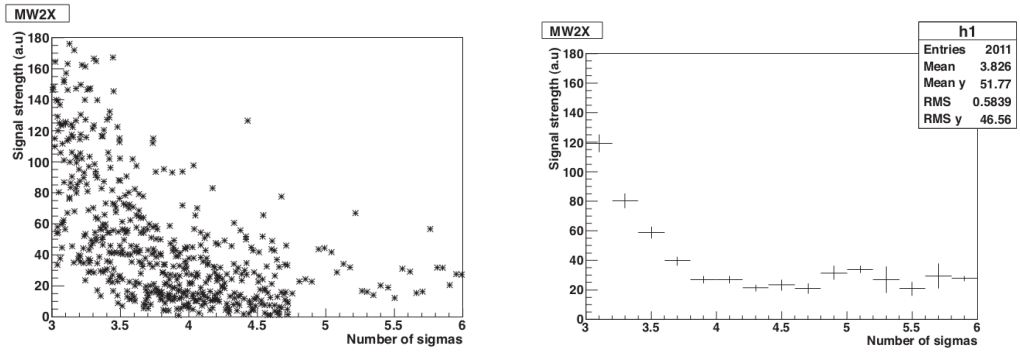

Figure 5.5: Data without binning (left) and data binned (right)

in most cases we performed the analysis for both sides of the halo in order to test this assumption.

5. Normalization factor in the parametrisation: For the parametrization of the halo we used the same parametrization as shown in Eq. **??** and Eq. **??**. However as the data taken is in signal strength, this data should be normalized to the number of particles by the following procedure.

First, we assume a function similar to Eq. **??** and Eq. **??** for the halo density distribution as a function of the number of σ:

$$\rho_{H,V} = AX^{-b} \tag{5.1}$$

where X corresponds to the number of σ and A is a constant. Assuming a Gaussian density distribution for the core, the maximum of this distribution normalized to the number of σ can be calculated as:

$$\rho_{max} = \frac{N}{\sqrt{2\pi}} \tag{5.2}$$

where N is the number of electrons in the beam. From the fitting of the data, we can obtain the signal strength as a function of the number of σ:

$$\bar{\rho}_{H,V} = aX^{-b} \tag{5.3}$$

where X corresponds to the number of σ and a is a constant given by the fit. The maximum signal strength measured is $\bar{\rho}_{max}$. Then, the ratio between the maximum

signal strength measured for the core, $\bar{\rho}_{max}$, and the amount of halo at 3σ, $\bar{\rho}_{H,V}$, in units of signal strength, has to be equal to the ratio of the number of particles of the core corresponding to the maximum of the Gaussian, ρ_{max}, and the amount of halo at 3 σ in units of number of particles, $\rho_{H,V}$:

$$\frac{\bar{\rho}_{H,V}}{\bar{\rho}_{max}} = \frac{\rho_{H,V}}{\rho_{max}} \tag{5.4}$$

Replacing Eq. 5.1 and Eq. 5.3 in Eq. 5.4 we can get a relation between the constants A and a:

$$A = \frac{Na}{\bar{\rho}_{max}\sqrt{2\pi}} \tag{5.5}$$

Then, the distribution to be compared with Suehara's parametrisation (Eq. **??** and Eq. **??**), independent on the number of particles, is:

$$\rho_{H,V}/N = (A/N)X^{-b} \tag{5.6}$$

where A can be calculated from Eq. 5.6.

In some particular cases we also fit the beam halo distribution measured by a Gaussian plus a constant function, as it is done in the ATF2 wire scanner control room software in normal operation to determine the beam core, using the following parametrization:

$$\rho_{H,V} = me^{\frac{-(X-n)^2}{2l^2}} + p \tag{5.7}$$

Then Eq. 5.7 is defined in units of number of particles and independent of N as:

$$\rho_{H,V}/N = (M/N)e^{\frac{-(X-n)^2}{2l^2}} + P/N \tag{5.8}$$

In the following section we will apply the analysis described for the different sets of data and compare the results with Suehara's parametrisation. However, when doing the comparison we have to take into account that the measurements done in 2005 were done for the old EXT line in ATF and the 2013 measurements have been done for the ATF2 beam line with stronger focusing optics and new elements with tighter apertures.

5.3.2 MW2X WS measurement results

Horizontal distribution

For this measurement we used the $50\mu m$ X wire to measure the horizontal beam halo. The combination of all the data after voltage normalisation is shown in Fig. 5.6 (upper). It can be seen that the data taken with 2000 V in the halo region has a large fluctuation due to the electronic noise. Therefore data binning is required to make the distribution more clear.

The left and right halo were fitted separately using the power function $\rho_H = aX^{-b}$ and the Gaussian plus linear fit $\rho_H = me^{\frac{-(X-n)^2}{2l^2}} + p$. Fig. 5.6 (lower) shows the fit for the right halo tail. The beam halo model obtained with the fit (2013 model) is compared with the beam halo model from 2005 measurements (2005 model). It can be noticed in Fig. 5.6 that beyond $5\sigma_x$ the distribution is flat and the dynamic range is less than 10^3.

The fit results are summarized in Table 5.2. The beam intensity here is $N = 7 \times 10^9$ electrons. It can be seen that the power factor for left and right beam halo distribution has a small difference, which indicates that the beam halo horizontal distribution may be asymmetric. This asymmetry was observed in the WS measurements done in 2005 also (see Fig. 3.15).

Vertical distribution

For this measurement we used the $10\mu m$ Y wire to measure the vertical beam halo. The combination of all the data after voltage normalisation is shown in Fig. 5.7 (upper). Similar to the horizontal distribution, large fluctuations can also be observed in the data taken with 2000 V in the halo region for the vertical distribution.

Fig. 5.7 (lower) shows the fit for the right halo tail. In this case beyond 5 σ_x the distribution observed is also flat. However, the dynamic range ($\sim 7 \times 10^3$) is a little bit higher than for the horizontal measurement using the $50\mu m$ x wire ($< 10^3$).

The fit results are summarized in Table 5.3. Comparing with the horizontal distribution, it can be seen that there is almost no difference between the left and right distribution, which may indicate a symmetric vertical distribution. Meanwhile, the power factor (~ -7) is twice that obtained in 2005, which means that the vertical beam halo population may be lower than in 2005 in the region of $3\sigma_y$ to $5\sigma_y$.

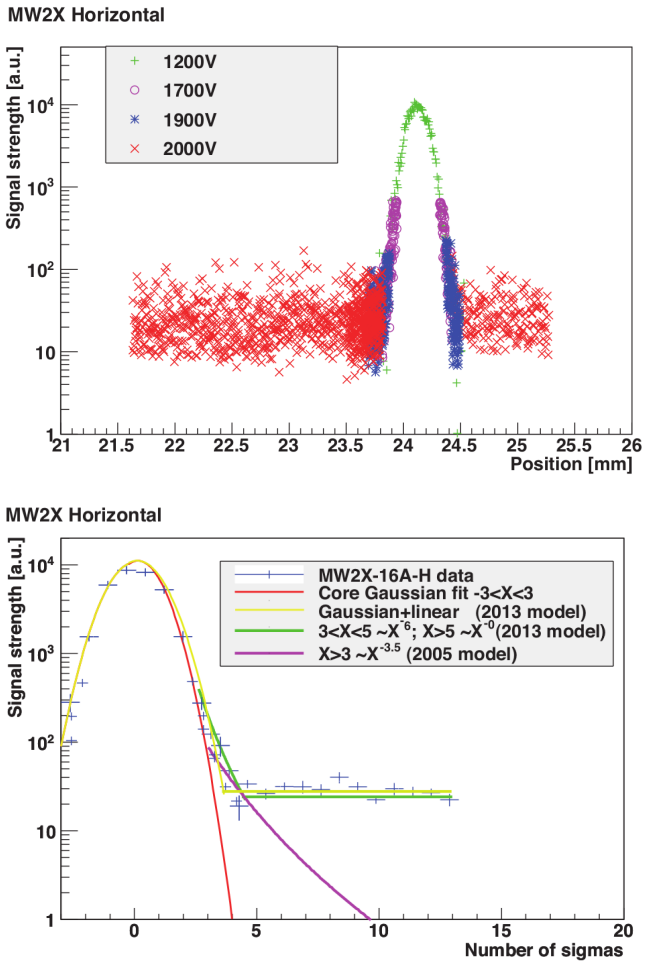

Figure 5.6: MW2X WS measured beam halo horizontal distribution

Model		χ^2	X $[\sigma]$
$\rho_H/N = (A/N)X^{-b}$	$\rho_{H,l}/N = (1.1 \pm 0.1)X^{-(4.8\pm0.1)}$	20	$3 < X < 5$
	$\rho_{H,r}/N = (2.8 \pm 1.2)X^{-(5.6\pm0.3)}$	8	
	$\rho_{H,l}/N = (0.0010 \pm 0.0001)X^{-(0\pm0.3)}$	2.3	$X > 5$
	$\rho_{H,r}/N = (0.0011 \pm 0.0001)X^{-(0.2\pm0.1)}$	0.6	
$\rho_H/N = (M/N)e^{-\frac{(X-n)^2}{2l^2}} +$ $+P/N$	$\rho_H/N = (0.89 \pm 0.01)e^{-\frac{(X-(0.12\pm0.01))^2}{2(0.96\pm0.01)^2}} +$ $+(0.107 \pm 0.001)$	2.4	$-30 < X < 15$

Table 5.2: MW2X-16A-H Modeling summary

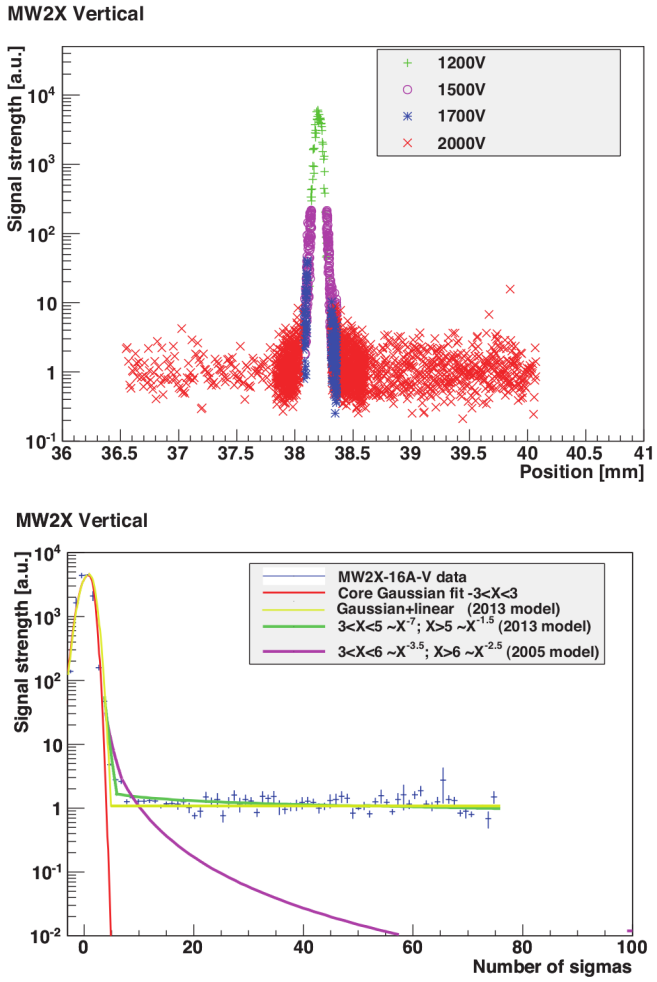

Figure 5.7: MW2X WS measured beam halo vertical distribution

Model		χ^2	X $[\sigma]$
$\rho_V/N = (A/N)X^{-b}$	$\rho_{V,l}/N = (9 \pm 5)X^{-(7.3\pm0.4)}$	1	$3 < X < 5$
	$\rho_{V,r}/N = (8 \pm 2)X^{-(7.2\pm0.2)}$	5.6	
	$\rho_{V,l}/N = (0.001 \pm 0.001)X^{-(1.1\pm0.3)}$	4.5	$X > 5$
	$\rho_{V,r}/N = (0.0010 \pm 0.0004)X^{-(1.0\pm0.1)}$	3	
$\rho_V/N = (M/N)e^{-\frac{(X-n)^2}{2l^2}} +$ $+P/N$	$\rho_V/N = (0.51 \pm 0.03)e^{-\frac{(X-(0.06\pm0.01))^2}{2(0.9\pm0.1)^2}} +$ $+(0.00005 \pm 0.00001)$	31	$-60 < X < 65$

Table 5.3: MW2X-16A-V Modeling summary

5.3.3 Post-IPW measurement results

Horizontal distribution

For this measurement we used the 50 μm X wire to measure the horizontal beam halo distribution. The combination of all the data after voltage normalisation is shown in Fig. 5.4 (lower). Data with fitting after binning is shown in Fig. 5.8. The fit of the beam core corresponds to the data taken at the lowest voltage (500 V). The fit results are summarized in Table 5.4. As the flat distribution start at $\sim 6\sigma_x$ fit of halo was done from $3\sigma_x$ to $6\sigma_x$. In this case the dynamic range also is very limited ($< 10^3$).

However, it can be seen from Fig. 5.8 that the measured horizontal distribution fits quite well with the 2005 model from $3\sigma_x$ to $6\sigma_x$. Nevertheless, since post-IPW is located after the IP, where large photon background can be generated for the detection, distribution beyond $6\sigma_x$ could not be measured using the post-IPW.

Vertical distribution

For this measurement we used the 50 μm Y wire to measure the vertical beam halo distribution. This wire is the first wire which interacts with the beam when the WS moves from downside to the upside (see Fig. 3.9). Therefore, we expect the background from other wires to be lower for the measurements using this wire especially on the downside of the beam (left side in the plots).

The combination of all the data after voltage normalisation and data binning is shown in Fig. 5.9 together with the enlarged fit of the right side distribution comparing with the 2005 model. The fit results are summarized in Table 5.5.

From the fit results, we could notice that the distribution of the halo is not symmetric. More halo is observed on the left side (downside of the beam) than the right side (upside of the beam). Meanwhile, from the upper plot in Fig. 5.9 an obvious edge of cut can be seen on the left side of the distribution at $\sim 14\sigma_y$ position. This cut could be caused by the TPB, where the β_y is relatively large. However more systematic measurements are needed to confirm this hypothesis. Therefore fit was done until $14\sigma_y$ on the left side before the edge of cut.

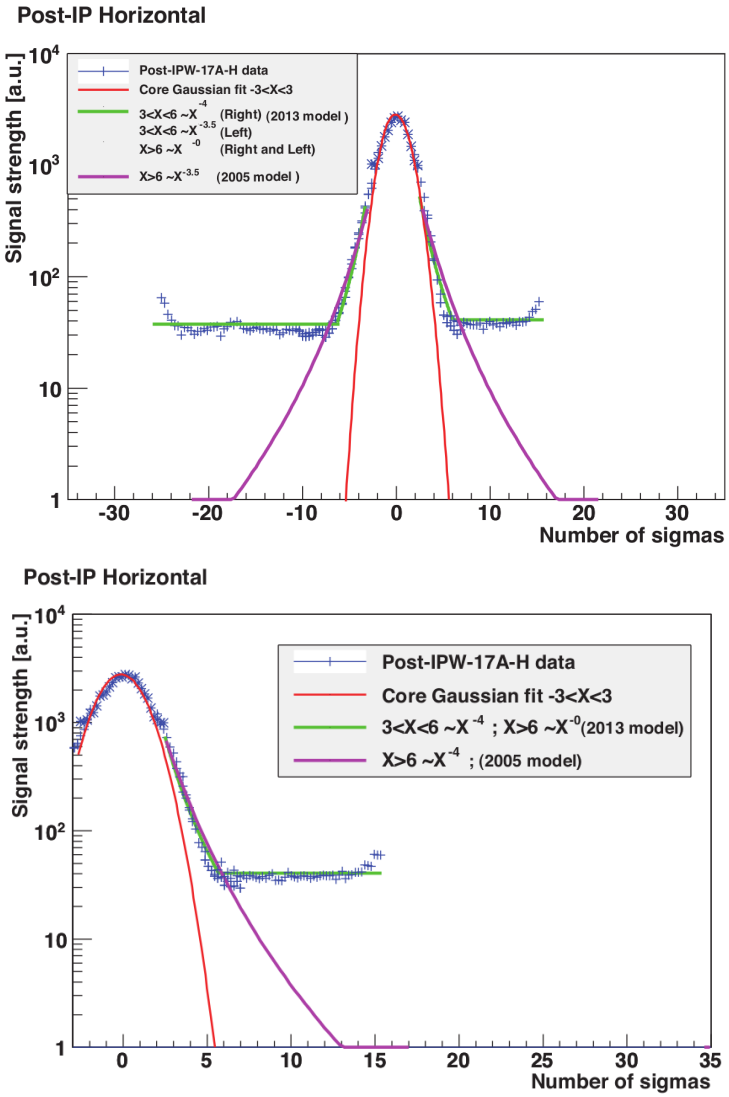

Figure 5.8: post-IPW measured horizontal beam halo distribution

Model		χ^2	X $[\sigma]$
$\rho_H/N = (A/N)X^{-b}$	$\rho_{H,l}/N = (6.2 \pm 0.8)X^{-(3.5\pm0.1)}$	4	$3 < X < 6$
	$\rho_{H,r}/N = (10.2 \pm 1.2)X^{-(4.2\pm0.1)}$	4.5	
	$\rho_{H,l}/N = (0.020 \pm 0.003)X^{-(0.002\pm0.02)}$	4	$X > 6$
	$\rho_{H,r}/N = (0.007 \pm 0.001)X^{-(0\pm0.02)}$	1.7	

Table 5.4: PostIPW-17A-H Modeling summary

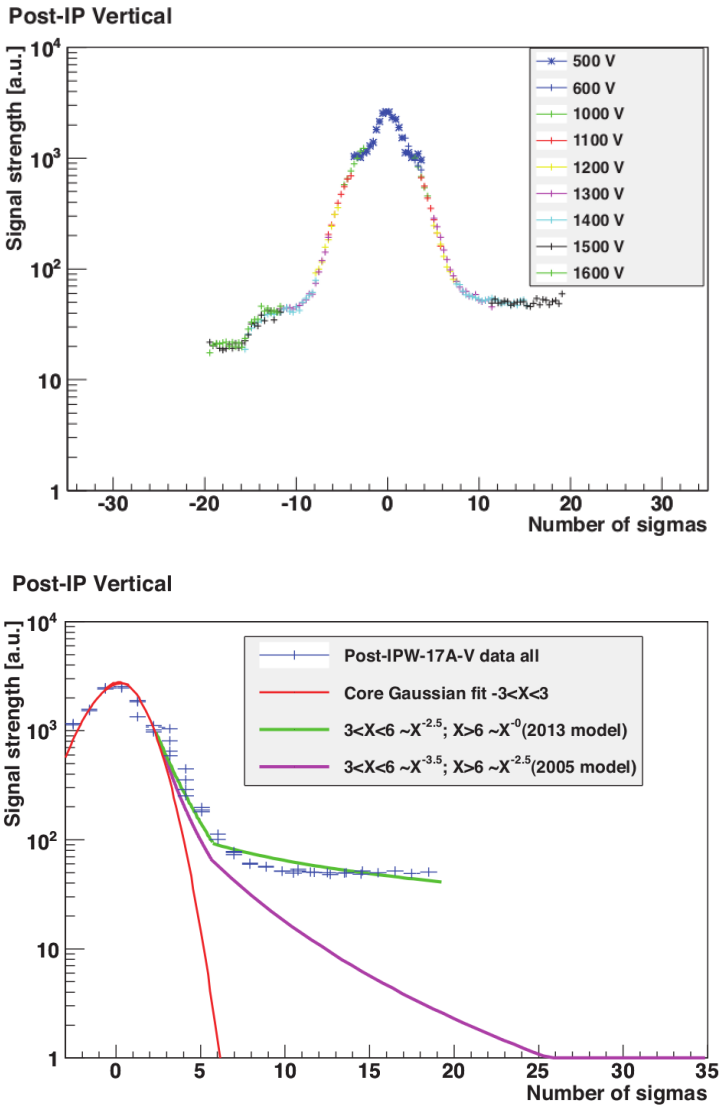

Figure 5.9: post-IPW measured vertical beam halo distribution

Model		χ^2	X $[\sigma]$
$\rho_V/N = (A/N)X^{-b}$	$\rho_{V,l} = (2.4 \pm 0.3)X^{-(1.9\pm0.1)}$	15	$3 < X < 6$
	$\rho_{V,r} = (4.9 \pm 0.4)X^{-(2.7\pm0.1)}$	11	
	$\rho_{V,l} = (11 \pm 3)X^{-(1.2\pm0.1)}$	76	$x > 6$
	$\rho_{V,r} = (0.5 \pm 0.2)X^{-(0.45\pm0.02)}$	50	

Table 5.5: PostIPW-17A-V Modeling summary

5.3.4 Beam halo as background for Shintake monitor

The BG monitor used for the post-IPW signal measurement is located about 10 cm upstream of the Shintake Monitor gamma-ray detector (a Cherenkov detector). Therefore, relating the beam halo distribution and background levels can be very useful in the context of background studies for the Shintake monitor.

As mentioned in Section 3.3.3, the main background are photons generated by the vertical beam halo hitting the final doublet and BDUMP bending magnets, and a TBP was installed 28 m upstream of the IP for the purpose of reducing this background. The half aperture of the TBP is 8 mm, which corresponds to a value of $\sim 27\sigma_y$ where the calculated $\sigma_y = 216.1\mu m$ as shown in Section 4.4. The post-IPW measured beam size is 293.5 μm and 314.7 μm for 17th April and 12th June 2013, respectively. Taken into account the mismatch factor (k) of σ_y between measurement and calculation given by the post-IPW :$k = \sigma_{measured}/\sigma_{calculated}$, the expected cut by TBP is at $\sim 19\sigma_y$ position. Since the TBP gives the tightest aperture upstream of the post-IPW (see Fig. **??**), the cut observed in the post-IPW measurements for vertical beam halo at $\sim 14\sigma_y$ in April and in June 2013 (see Fig. 5.10) could be given by the aperture of TBP, and the asymmetric distribution could be correlated to the position of TBP.

As the location of the TBP has 3π phase difference with the post-IPW (see Table 3.2), the effect of the TBP movement on the beam halo distribution can be investigated by the beam halo measurements using the post-IPW. Therefore, we performed a series of measurements moving the TBP vertically. Fig. 5.11 (upper) shows the beam halo distribution measured with the post-IPW corresponding to different TBP positions. Taking into account the 3π phase difference, the upside of the beam at TBP location represents the downside of the beam at the post-IPW location (left side of the plot). Therefore, by moving the TBP up, we would expect to observe more halo on the downside of the beam, whereas, by moving the TBP down, we would expect to observe less halo on the downside of the beam at the post-IPW location.

However, what we observed is not the same as what we expected. From Fig. 5.11 (upper) it can be seen that by moving the TBP up by 1 mm, we observe less beam halo on the downside of the beam and slightly more halo on the upside of the beam at the post-IPW location; By moving the TBP down by 0.5 mm, we observe more beam halo on both side of the beam. This different behaviour between moving the TBP up and

down may indicate an asymmetry beam halo distribution at the TBP position. This difference was the motivation of installing the TBP as a shield against the background at the IPBSM. However, the sources of the asymmetric beam halo distribution are unknown.

The change of background level during the movement of the TBP was measured both with BG monitor and with the Cherenkov detector. The measured background level while moving the TBP is shown in Fig. 5.11 (lower). It can be seen that the BG level measured is quite consistent with the change of beam halo level. The background level is slightly decreased by moving the TBP up from 0 mm up to 3 mm, however, moving the TBP down caused large increase of background level. This confirms the measured beam halo distributions in Fig. 5.11. However, the reasons for the difference between the expected and the observed changes of beam halo distribution are unknown.

During the measurement using Shintake monitor, the TBP can be moved both horizontally and vertically to find the optimised position with minimum background level. However, as the TBP is not a "real" collimator for beam halo, it can reduce the background only by a relatively small amount. Therefore, another collimator system is utilised 6.2 m downstream of the IP to collimate the bremsstrahlung photons. However, as discussed in Section 3.4.3, to further improve the performance of IPBSM, a dedicated collimator device is required to collimate the beam halo at the upstream of the IP [97]. This device is under design, the design parameters will be defined according to the current measured beam halo distributions and the requirement for Compton signal measurements. Thus, precise measurements of beam halo using DS with a large dynamic range are of great importance. This studies could be perform in the future in a systematic way with a dedicated collimator device.

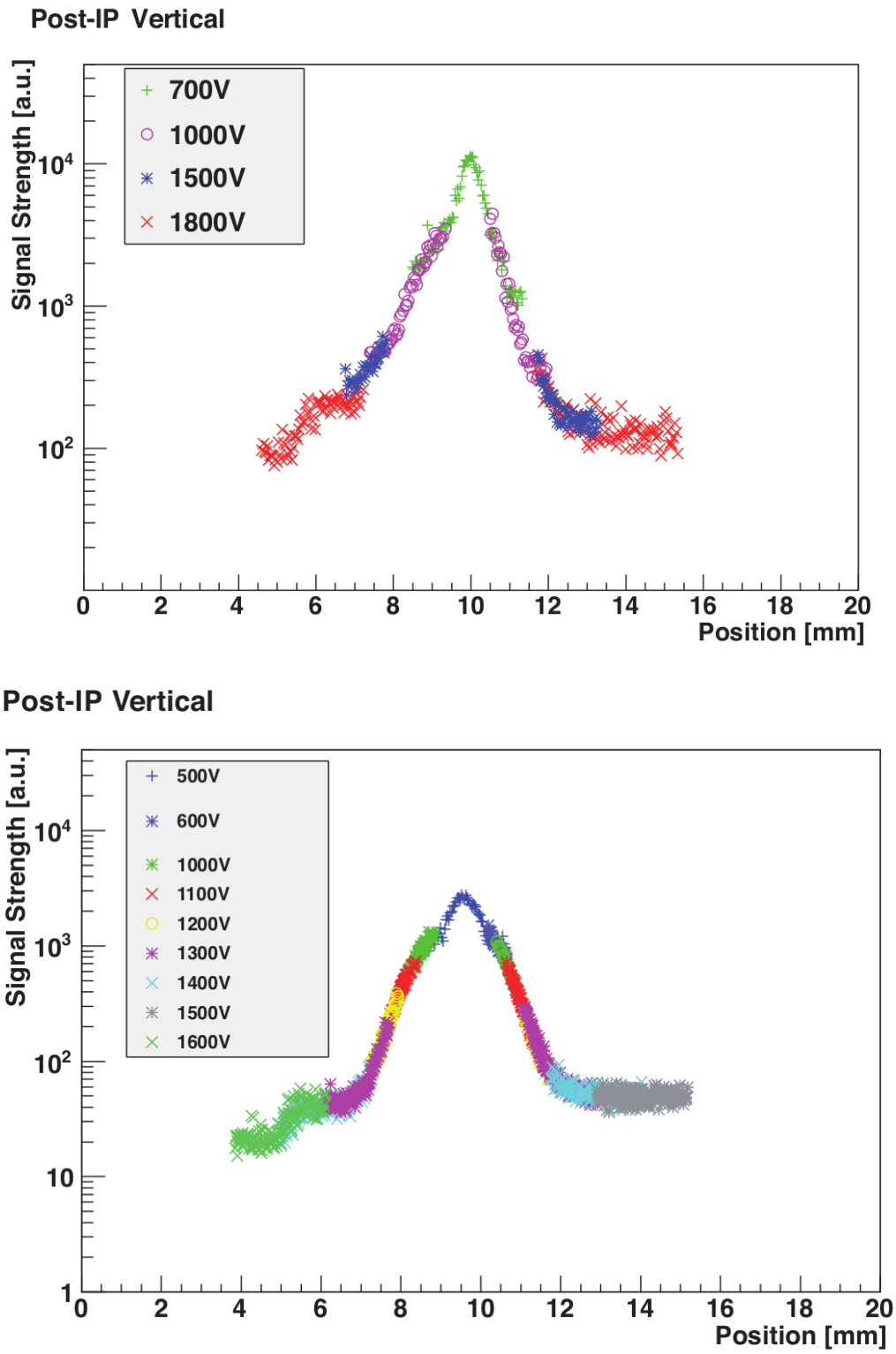

Figure 5.10: post-IPW measured vertical beam halo distribution in 17th April (left) and 12th June (right) 2013

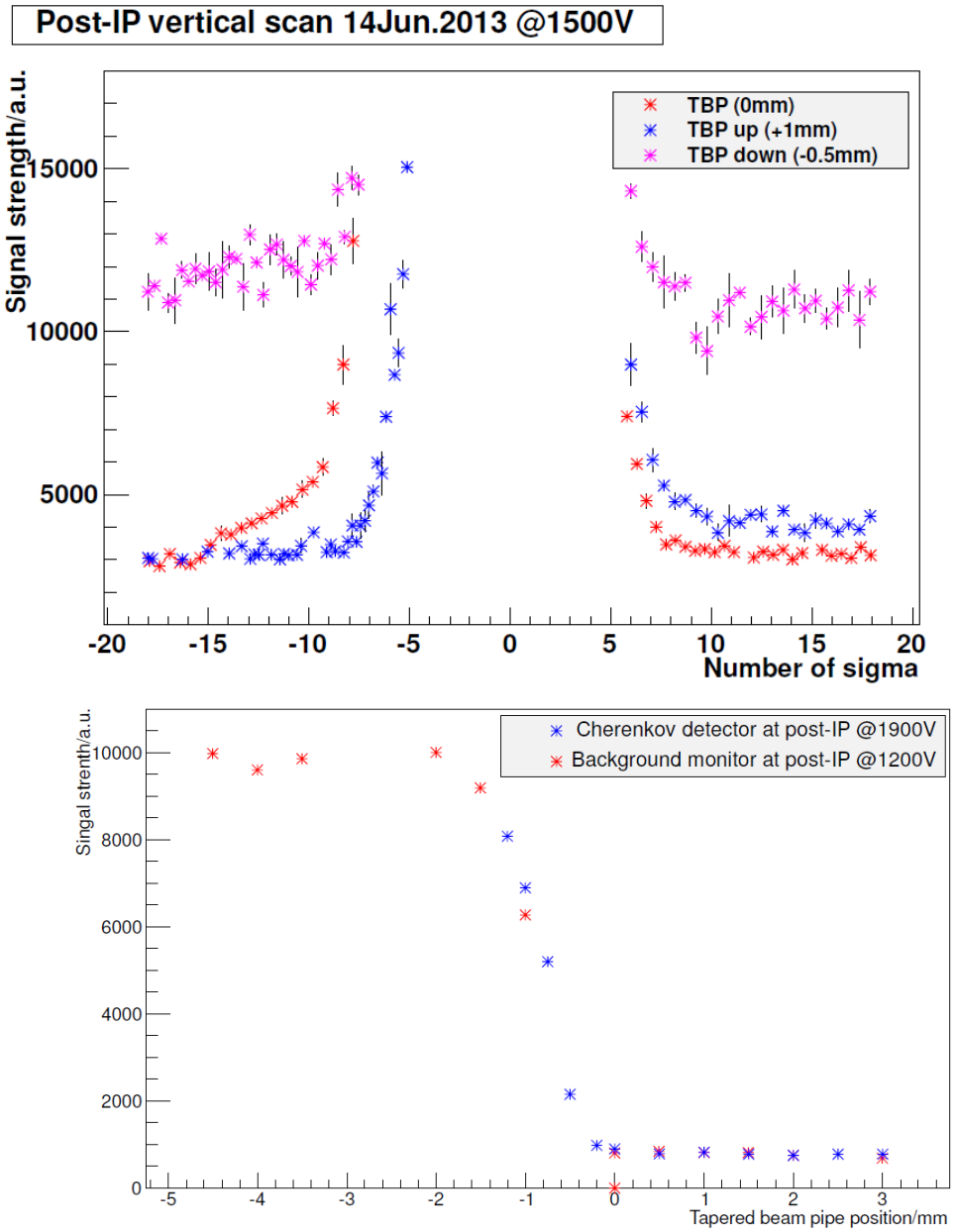

Figure 5.11: post-IPW measured beam halo distribution with different TBP positions (upper);Background level measured by the background monitor and Cherenkov detector at the Post-IP for different TBP position (lower): 0 mm represent the stay position of TBP, positive and negative positions represent moving the TBP up and down respectively